



An Extreme X-Ray Variability Event of a Weak-line Quasar

Q. Ni^{1,2}, W. N. Brandt^{1,2,3}, W. Yi^{1,4,5}, B. Luo^{6,7,8}, J. D. Timlin, III^{1,2}, P. B. Hall⁹, Hezhen Liu^{6,7,8},
R. M. Plotkin¹⁰, O. Shemmer¹¹, F. Vito^{12,13}, and Jianfeng Wu¹⁴

¹ Department of Astronomy & Astrophysics, The Pennsylvania State University, 525 Davey Lab, University Park, PA 16802, USA; qxn1@psu.edu

² Institute for Gravitation and the Cosmos, The Pennsylvania State University, University Park, PA 16802, USA

³ Department of Physics, The Pennsylvania State University, University Park, PA 16802, USA

⁴ Yunnan Observatories, Kunming, 650216, People's Republic of China

⁵ Key Laboratory for the Structure and Evolution of Celestial Objects, Chinese Academy of Sciences, Kunming 650216, People's Republic of China

⁶ School of Astronomy and Space Science, Nanjing University, Nanjing, Jiangsu 210093, People's Republic of China

⁷ Key Laboratory of Modern Astronomy and Astrophysics (Nanjing University), Ministry of Education, Nanjing, Jiangsu 210093, People's Republic of China

⁸ Collaborative Innovation Center of Modern Astronomy and Space Exploration, Nanjing 210093, People's Republic of China

⁹ Department of Physics & Astronomy, York University, 4700 Keele Street, Toronto, ON M3J 1P3, Canada

¹⁰ Department of Physics, University of Nevada, 1664 N. Virginia Street, Reno, NV 89557, USA

¹¹ Department of Physics, University of North Texas, Denton, TX 76203, USA

¹² Instituto de Astrofísica and Centro de Astroingeniería, Facultad de Física, Pontificia Universidad Católica de Chile, Casilla 306, Santiago 22, Chile

¹³ Chinese Academy of Sciences South America Center for Astronomy, National Astronomical Observatories, CAS, Beijing 100012, People's Republic of China

¹⁴ Department of Astronomy, Xiamen University, Xiamen, Fujian 361005, People's Republic of China

Received 2019 December 13; revised 2020 January 14; accepted 2020 January 20; published 2020 February 3

Abstract

We report the discovery of an extreme X-ray flux rise (by a factor of $\gtrsim 20$) of the weak-line quasar Sloan Digital Sky Survey (SDSS) J153913.47+395423.4 (hereafter SDSS J1539+3954) at $z = 1.935$. SDSS J1539+3954 is the most-luminous object among radio-quiet type 1 active galactic nuclei (AGNs) where such dramatic X-ray variability has been observed. Before the X-ray flux rise, SDSS J1539+3954 appeared X-ray weak compared with the expectation from its ultraviolet (UV) flux; after the rise, the ratio of its X-ray flux and UV flux is consistent with the majority of the AGN population. We also present a contemporaneous HET spectrum of SDSS J1539+3954, which demonstrates that its UV continuum level remains generally unchanged despite the dramatic increase in the X-ray flux, and its C IV emission line remains weak. The dramatic change only observed in the X-ray flux is consistent with a shielding model, where a thick inner accretion disk can block our line of sight to the central X-ray source. This thick inner accretion disk can also block the nuclear ionizing photons from reaching the high-ionization broad emission-line region, so that weak high-ionization emission lines are observed. Under this scenario, the extreme X-ray variability event may be caused by slight variations in the thickness of the disk. This event might also be explained by gravitational light-bending effects in a reflection model.

Unified Astronomy Thesaurus concepts: X-ray active galactic nuclei (2035); Active galaxies (17); Quasars (1319); X-ray quasars (1821); Radio quiet quasars (1354); X-ray sources (1822)

1. Introduction

Weak-line quasars (WLQs; e.g., Fan et al. 1999; Diamond-Stanic et al. 2009; Plotkin et al. 2010) are a notable group of active galactic nuclei (AGNs) largely discovered by the Sloan Digital Sky Survey (SDSS; York et al. 2000). While typical quasars show strong and broad line emission in the optical/ultraviolet (UV), WLQs are type 1, radio-quiet quasars with weak or no emission lines. WLQs with C IV rest-frame equivalent widths (REWs) $\lesssim 10 \text{ \AA}$ deviate negatively at $\gtrsim 3\sigma$ levels from the mean C IV REW of SDSS quasars; at the same time, there is no such population that deviates positively at $\gtrsim 3\sigma$ levels from the mean of the C IV REW distribution (e.g., Diamond-Stanic et al. 2009; Wu et al. 2012).

WLQs have also exhibited remarkable X-ray properties. For typical radio-quiet quasars without broad absorption lines (BALs), the X-ray-to-optical power-law slope parameter (α_{ox})¹⁵ follows a correlation with 2500 Å monochromatic luminosity ($L_{2500 \text{ \AA}}$; e.g., Steffen et al. 2006; Just et al. 2007; Lusso & Risaliti 2016). However, about half of the WLQs have notably lower X-ray luminosities compared to the expectation from the $\alpha_{\text{ox}}-L_{2500 \text{ \AA}}$ relation (e.g., Luo et al. 2015; Ni et al.

2018). For this half of the WLQ population, high apparent levels of intrinsic X-ray absorption, Compton reflection, and/or scattering have been suggested through X-ray stacking and spectral analyses (e.g., Wu et al. 2011, 2012; Luo et al. 2015; Ni et al. 2018). Also, the notably steep X-ray spectra of the other half of the WLQ population that is not X-ray weak indicate accretion at high Eddington ratios (e.g., Luo et al. 2015; Marlar et al. 2018).

However, WLQs have not generally been associated with extreme X-ray variability before. For typical AGNs, the long-term variation of X-ray luminosity is generally within a factor of ≈ 2 , and seldom exceeds a factor of ≈ 10 (e.g., Gibson & Brandt 2012; Yang et al. 2016; Middei et al. 2017). Also, the anticorrelation between the X-ray variability amplitude and the black hole mass (e.g., Ponti et al. 2012) suggests that extreme X-ray variability is not generally expected among luminous quasars that tend to host high-mass black holes (e.g., Shen & Kelly 2012). Extreme X-ray variability events (X-ray luminosity variations by factors of $\gtrsim 10$) have been found among radio-loud AGNs that have jet-linked X-ray variability (e.g., Carnerero et al. 2017), BAL quasars that have absorption-linked X-ray variability (e.g., Saez et al. 2012), and changing-look AGNs that exhibit multiwavelength variability (e.g., Oknyansky et al. 2019). There are also extreme X-ray

¹⁵ α_{ox} is the power-law slope connecting the monochromatic luminosities at rest-frame 2500 Å and 2 keV; $\alpha_{\text{ox}} = 0.384 \log(L_{2 \text{ keV}}/L_{2500 \text{ \AA}})$.

Table 1
X-Ray Observations and Derived Properties of SDSS J1539+3954

Observation ID	Observation Start Date	Exposure Time	Soft-band Counts	Hard-band Counts	Band Ratio	Γ_{eff}	$f_{2\text{ keV}}$	α_{ox}	$\Delta\alpha_{\text{ox}}(\sigma)$
(1)	(2)	(3)	(4)	(5)	(6)	(7)	(8)	(9)	(10)
14948	2013 Dec 13	5.3	<2.4	<2.5	<0.83	<-2.18	<-0.46 (3.17)
22528	2019 Sep 12	7.3	$29.1^{+6.6}_{-5.5}$	$15.2^{+5.3}_{-4.1}$	$0.52^{+0.21}_{-0.14}$	$2.0^{+0.4}_{-0.4}$	16.58	-1.68	0.04 (0.26)

Note. (1) *Chandra* observation ID. (2) Observation start date. (3) Background-flare cleaned effective exposure time in the 0.5–8 keV band in units of ks. (4)/(5) Aperture-corrected source counts in the soft (0.5–2 keV)/hard (2–8 keV) band. An upper limit at a 90% confidence level is given if the source is not detected. (6) Ratio between the soft-band and hard-band counts. “...” indicates that the source is undetected in both bands. (7) 0.5–8 keV effective power-law photon index. “...” indicates that Γ_{eff} cannot be constrained. (8) Rest-frame 2 keV flux density in units of 10^{-32} erg cm $^{-2}$ s $^{-1}$ Hz $^{-1}$. (9) Measured α_{ox} values. (10) Difference between the measured α_{ox} and the expected α_{ox} from the Just et al. (2007) $\alpha_{\text{ox}}-L_{2500\text{ \AA}}$ relation. The statistical significance of this difference measured following Table 5 of Steffen et al. (2006) is given in parentheses.

variability events among radio-quiet non-BAL AGNs that do not have simultaneous changes in the UV/optical. These events have mostly been associated with narrow-line Seyfert 1 galaxies that have small black hole masses (e.g., Liu et al. 2019).

In this Letter, we report the discovery of an extreme X-ray variability event of a radio-quiet non-BAL WLQ, SDSS J153913.47+395423.4 (hereafter SDSS J1539+3954) at $z = 1.935$. SDSS J1539+3954 is a WLQ selected in Plotkin et al. (2010) for its weak C IV emission features. It has a bolometric luminosity of $L_{\text{bol}} \approx 1.5 \times 10^{47}$ erg s $^{-1}$ (Shen et al. 2011), which makes it the most-luminous radio-quiet AGN showing extreme X-ray variability.

2. Observations and Data Analyses

In Section 2.1, we present the two *Chandra* X-ray observations obtained for SDSS J1539+3954 that exhibit strong variation in the X-ray flux level; in Section 2.2, we present all the optical spectroscopic observations for SDSS J1539+3954 that are generally consistent.

2.1. Chandra X-Ray Observation and Data Analyses

We list in Table 1 the two X-ray observations of SDSS J1539+3954. These *Chandra* observations were performed with the Advanced CCD Imaging Spectrometer spectroscopic array (ACIS-S; Garmire et al. 2003) in VFaint mode. The new *Chandra* Cycle 21 observation is a part of our program to obtain deeper X-ray coverage for a set of WLQs (PI: W. N. Brandt).

We processed the *Chandra* data using the *Chandra* Interactive Analysis of Observations (CIAO) tools (Fruscione et al. 2006), following the steps in Luo et al. (2015) and Ni et al. (2018). We first used the CHANDRA_REPRO script and the DEFLARE script to create the cleaned event file, and then created images in the 0.5–2 keV (soft), 2–8 keV (hard), and 0.5–8 keV (full) bands. Source positions are determined by WAVDETECT. In case of non-detection (see Section 3 of Ni et al. 2018 for the definition of non-detection), we adopt the SDSS position. We performed aperture photometry in both the soft band and hard band: source counts were extracted from a 2'' radius circular aperture centered on the source position, and background counts were extracted from a source-free annular region with a 10'' inner radius and a 40'' outer radius. When the source is undetected, the upper limits on the source counts were derived using the 90% confidence-level table in Kraft et al. (1991). As we can see in Figure 1(a), SDSS J1539+3954 was

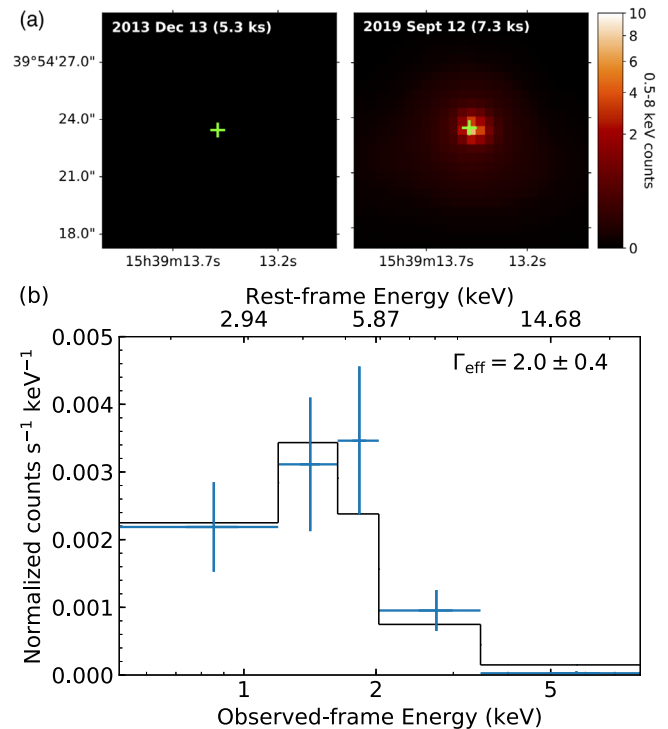


Figure 1. (a) *Chandra* full-band (0.5–8 keV) images of SDSS J1539+3954 in two different epochs (smoothed with CSMOOTH). SDSS J1539+3954 was not detected in 2013 (see the left panel), and was detected with ≈ 44 counts in 2019 (see the right panel). (b) The full-band X-ray spectrum of SDSS J1539+3954 from the 2019 *Chandra* observation (adjacent bins are combined until they provide a detection at a $>3\sigma$ level for presentation purposes), shown with a folded *phabs***powerlaw* model in XSPEC.

not detected in the first 5.3 ks *Chandra* observation, and was detected with ≈ 44 counts in total in the second 7.3 ks *Chandra* observation.

2.2. Spectroscopic Observations and Data Analyses

We list in Table 2 all the optical spectroscopic observations of SDSS J1539+3954. SDSS J1539+3954 was observed by SDSS-I/II on 2004 June 15, and the Baryon Oscillation Spectroscopic Survey of SDSS-III (BOSS; Dawson et al. 2013) on 2012 April 29. The reduced SDSS and BOSS spectra were downloaded directly from the SDSS data archive.

After SDSS J1539+3954 was found to exhibit large X-ray variability, we promptly observed this object again with the Low-resolution Spectrograph-2 (LRS2; Chonis et al. 2014) on the Hobby–Eberly Telescope (HET; Ramsey et al. 1998). The

Table 2
Spectroscopic Observations of SDSS J1539+3954 and the Measured UV Emission-line Properties

Date	Instrument	Spectral Coverage	Exposure Time	S/N	C IV REW	C IV Blueshift	C IV FWHM
(1)	(2)	(\AA)	(s)	(5)	(\AA)	(km s^{-1})	(km s^{-1})
		(3)	(4)		(6)	(7)	(8)
2004 Jun 15	SDSS	3800–9200	2700	25.6	7.6 ± 1.3	5230 ± 670	11570 ± 790
2012 Apr 29	BOSS	3650–10400	2700	30.4	8.2 ± 0.9	5230 ± 910	12320 ± 530
2019 Sep 20	HET/LRS2-B	3700–7000	1500	30.0	4.9 ± 1.5	4900 ± 400	10210 ± 540
2019 Sep 24	HET/LRS2-R	6500–10500	1140	12.3

Note. (1) Date of the spectroscopic observation. (2) Name of the instrument. (3) Observed-frame spectral coverage of the instrument. (4) Total exposure time in seconds. (5) The average S/N at $\lambda_{\text{rest}} = 1750\text{--}1800 \text{\AA}$ for SDSS, BOSS, and HET/LRS2-B spectra, and at $\lambda_{\text{rest}} = 2650\text{--}2700 \text{\AA}$ for the HET/LRS2-R spectrum. (6)/(7)/(8) REW/blueshift/FWHM of the C IV $\lambda 1549$ emission line. “...” indicates that the C IV emission line is not covered in the spectrum.

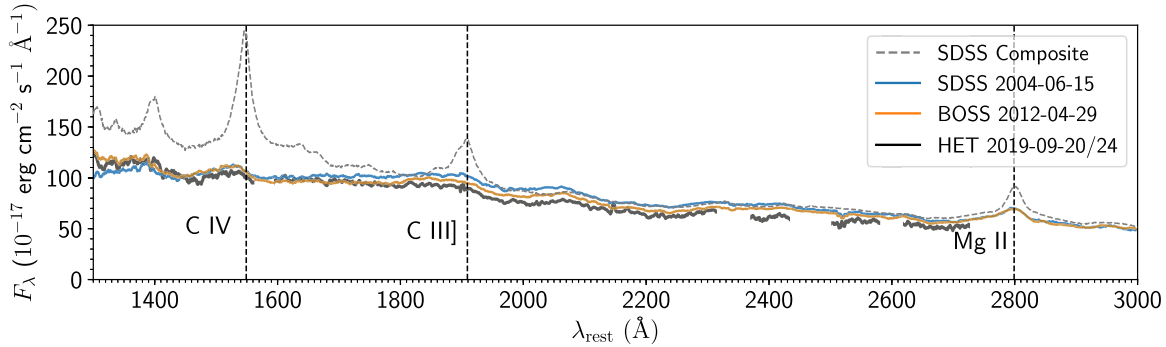


Figure 2. HET spectrum of SDSS J1539+3954 taken $\approx 2.7/4.1$ rest-frame days after the discovery of the extreme X-ray variability event (displayed together with the earlier SDSS spectra). We mask the areas where the HET spectrum suffers from channel discontinuities and telluric absorption (G. Zeimann 2019, private communication). In general, the UV continuum and emission-line properties do not exhibit significant changes as in the X-ray. The SDSS quasar composite spectrum from Vanden Berk et al. (2001) is scaled to the 2004 SDSS spectrum of SDSS J1539+3954 at rest-frame 2240\AA and plotted in the background for comparison.

observation with the blue arm of LRS2 (LRS2-B) was performed 8 days (≈ 2.7 days in the rest frame) after the *Chandra* observation, and the observation with the red arm of LRS2 (LRS2-R) was performed 12 days (≈ 4.1 days in the rest frame) after the *Chandra* observation. The LRS2 spectra were reduced with the HET pipeline *panacea*.¹⁶ The current version of the HET pipeline cannot correct for telluric absorption, and there are still some channel discontinuities. The flux calibration is estimated to have an uncertainty around 20% (G. Zeimann 2019, private communication). However, it is still sufficient for us to probe the basic properties of the UV continuum and emission lines. In Figure 2, we display all the spectra obtained for SDSS J1539+3954 together. They do not show noticeable variations.

3. Results

3.1. X-Ray Properties

For the new *Chandra* detection (≈ 44 counts) of SDSS J1539+3954, we calculated the band ratio (the ratio of hard-band counts to soft-band counts) and its uncertainty with the code BEHR (Park et al. 2006). Assuming a power-law spectrum modified by Galactic absorption, we use the Portable, Interactive, Multi-mission Simulator (PIMMS)¹⁷ to derive the $0.5\text{--}8 \text{ keV}$ effective power-law photon index (Γ_{eff}) and its uncertainty from the band ratio. We have also performed a power-law fit with XSPEC (Arnaud 1996) using the Cash statistic (Cash 1979) and obtained consistent results (see

Figure 1(b) for the X-ray spectrum). The results are listed in Table 1. The Γ_{eff} value of SDSS J1539+3954 is consistent with that of typical luminous radio-quiet quasars ($\Gamma_{\text{eff}} = 1.8\text{--}2.0$; e.g., Reeves et al. 1997; Shemmer et al. 2005; Just et al. 2007; Scott et al. 2011). We then derived the unabsorbed soft-band flux (which covers rest-frame 2 keV) with PIMMS from the soft-band net count rate and Γ_{eff} , and calculated the rest-frame 2 keV flux density ($f_{2 \text{ keV}}$) from the flux and Γ_{eff} . In the case of X-ray non-detection, we could set an upper limit on $f_{2 \text{ keV}}$ following the same method using the upper limit for the soft-band net count rate and $\Gamma_{\text{eff}} = 2.0$ adopted from the case of X-ray detection. As can be seen in Table 1, $f_{2 \text{ keV}}$ varied by a factor of $\gtrsim 20$ between the two epochs. We note that different reasonable assumptions for the Γ_{eff} value ($\Gamma_{\text{eff}} \approx 1.6\text{--}2.4$) in the case of X-ray non-detection will not substantially change the results, and the variation in $f_{2 \text{ keV}}$ is always extreme (by a factor of $\gtrsim 17\text{--}24$).

3.2. UV Emission-line and Continuum Properties

In Figure 2, we can see that the UV continuum level and emission-line profiles of SDSS J1539+3954 remain generally unchanged from 2004 to 2019, considering the flux uncertainty of the HET spectrum. Our measurement of the redshift $z = 1.935 \pm 0.004$ based on the Mg II line in the SDSS and BOSS spectra is consistent with the value reported in Luo et al. (2015). Here, the adopted redshift is the average of two measurement results (from the two spectra); the uncertainty is the difference between two measurements. We measured the C IV REW, blueshift, and FWHM in the three different epochs, as C IV properties are found to be linked with X-ray weakness among typical quasars (e.g., Gibson et al. 2008; Timlin et al.

¹⁶ <https://github.com/grzeimann/Panacea>
¹⁷ <https://cxc.harvard.edu/toolkit/pimms.jsp>

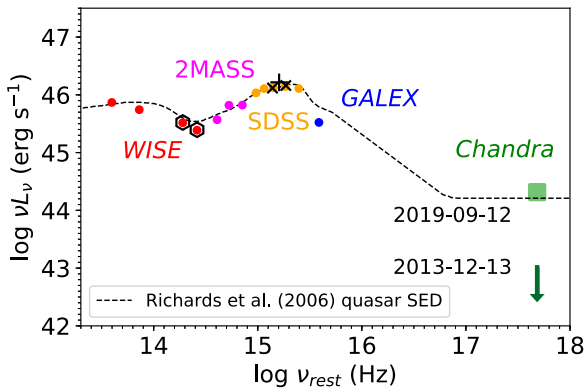


Figure 3. SED of SDSS J1539+3954. The SED was scaled at rest-frame 3000 Å to the composite SED (dashed line) of optically luminous quasars from Richards et al. (2006) by a factor of ≈ 0.3 . IR-to-UV SED data from *WISE*, *2MASS*, *SDSS*, and *GALEX* are represented by red, magenta, orange, and blue points. The blue data point from *GALEX* NUV falls below the composite SED due to Ly α absorption. The black crosses come from ZTF, the black plus comes from CRTS, and the black hexagons come from NEOWISE; the error bars showing the standard deviations of observed luminosities during the available monitoring are too small to be visible. The green square shows the rest-frame 2 keV luminosity of SDSS J1539+3954 in 2019 from *Chandra*; the green arrow shows the rest-frame 2 keV luminosity upper limit (90% confidence) of SDSS J1539+3954 in 2013 from *Chandra*.

2020). For each spectrum, we performed both the local and global continuum fits following Yi et al. (2019). For the local continuum fit, we fit a power-law function to the two “anchor” regions located on the blue/red-wing ends of the C IV emission line; for the global continuum fit, we model the continuum with a reddened power-law function to fit spectral windows that are relatively free of emission/absorption features. After subtracting the fitted continuum, we fit the C IV emission with two Gaussian components to measure its REW, blueshift, and FWHM. The REW is calculated from the fitted profile normalized by the continuum; the blueshift is converted from the wavelength bisecting the cumulative total flux of the C IV emission; the FWHM is derived from the combination of the two fitted Gaussian components. The reported C IV REW, blueshift, and FWHM values are the mean values generated by the two different continuum-fitting methods, and the reported uncertainties are the combination of the uncertainty from Monte Carlo simulations and the difference between the two methods. The measurement results are shown in Table 2. We can see that the C IV emission-line properties do not have significant variations in the three different epochs. While the X-ray flux of SDSS J1539+3954 has experienced a dramatic increase, it remains a WLQ.

3.3. The Multiwavelength Spectral Energy Distribution (SED) and X-Ray-to-optical Properties

In Figure 3, we display the multiwavelength SED of SDSS J1539+3954, showing photometric data collected by the *Wide-field Infrared Survey Explorer* (*WISE*; Wright et al. 2010), *Two Micron All Sky Survey* (*2MASS*; Skrutskie et al. 2006), *SDSS*, *Galaxy Evolution Explorer* (*GALEX*; Martin et al. 2005), and *Chandra*, as well as the *Catalina Real-time Transient Survey* (*CRTS*; Drake et al. 2009), *Zwicky Transient Facility* (*ZTF*; Bellm et al. 2019), and *Near-Earth Object Wide-field Infrared Survey Explorer* project (*NEOWISE*; Mainzer et al. 2014). *CRTS* monitored SDSS J1539+3954 from 2005 July 1 to 2013 September 28 (which is ≈ 2.5 months before the first *Chandra*

observation of SDSS J1539+3954), and the results are reported in the *V* band (≈ 1870 Å in the rest frame); the Data Release 2 of ZTF includes the light curves of SDSS J1539+3954 from 2018 March to 2019 June in both the *g* band and the *r* band (≈ 1610 Å and 2160 Å in the rest frame); the 2019 data release of NEOWISE contains the light curves of SDSS J1539+3954 from 2014 to 2018 at 3.4 μm and 4.6 μm (≈ 1.1 and 1.6 μm in the rest frame). No remarkable flux variation is detected by *CRTS*, ZTF, or NEOWISE, though we do observe modest variability in the ZTF and NEOWISE light curves (e.g., the ZTF light curves show variability of $\lesssim 0.1$ mag).¹⁸ The IR-to-UV SED of SDSS J1539+3954 is similar to those of typical quasars. The X-ray luminosity of SDSS J1539+3954 from the first *Chandra* observation is much lower than that of the composite SED of luminous quasars (Richards et al. 2006); the X-ray luminosity from the recent *Chandra* observation is roughly consistent with the composite SED.

We measured the α_{ox} parameter for SDSS J1539+3954 in the two different X-ray epochs (see Footnote 1 for the equation). As discussed before, the UV luminosity of SDSS J1539+3954 does not exhibit significant variability during the long-term monitoring, and the spectroscopic observations of SDSS J1539+3954 in three different epochs show a roughly consistent UV continuum level. Thus, when calculating α_{ox} , we adopt the $f_{2500 \text{ \AA}}$ value measured from the SDSS spectrum (Shen et al. 2011) for the two different X-ray epochs consistently. With the $f_{2 \text{ keV}}$ value/upper limit obtained in Section 3.1, we can calculate the α_{ox} value/upper limit for the two epochs. From the empirical $\alpha_{\text{ox}}-L_{2500 \text{ \AA}}$ relation for typical quasars (e.g., Just et al. 2007), we derived an expected value of α_{ox} for SDSS J1539+3954. Then, we measured the difference between the observed α_{ox} and the expected α_{ox} as $\Delta\alpha_{\text{ox}}$. The α_{ox} and $\Delta\alpha_{\text{ox}}$ results are listed in Table 1. $\Delta\alpha_{\text{ox}}$ provides a measurement of X-ray weakness compared with the expected X-ray flux, as the ratio between the observed X-ray flux and expected X-ray flux is simply $10^{\Delta\alpha_{\text{ox}}/0.384}$. The first *Chandra* observation of SDSS J1539+3954 demonstrates that it is X-ray weak by a factor of ≈ 16 , and the second *Chandra* observation shows that SDSS J1539+3954 now follows the empirical $\alpha_{\text{ox}}-L_{2500 \text{ \AA}}$ relation well (lying $\approx 0.3\sigma$ above the relation).¹⁹

4. Discussion

4.1. The Second Discovery of Extreme X-Ray Variability among WLQs

The extreme X-ray variability discovered from SDSS J1539+3954 is the second example of extreme X-ray variability among WLQs. PHL 1092 is a $z = 0.40$ radio-quiet quasar with $\log L_{\text{bol}} \approx 46.65$, and it was the first WLQ found to exhibit extreme X-ray variability (by a factor of ≈ 260 ; e.g., Miniutti et al. 2012). As summarized in Liu et al. (2019), at high luminosities ($L_{\text{bol}} > 10^{46}$ erg s^{-1}), PHL 1092 was the only

¹⁸ The mean and standard deviation of the recorded *CRTS* *V*-band/*ZTF* *g*-band/*ZTF* *r*-band/*NEOWISE* 3.6 μm /*NEOWISE* 4.5 μm magnitudes are $\approx 17.40 \pm 0.07/17.69 \pm 0.03/17.49 \pm 0.03/17.48 \pm 0.10/16.82 \pm 0.11$. These standard-deviation values are comparable to the mean measurement uncertainties in these five bands (0.09/0.03/0.02/0.09/0.11).

¹⁹ Alternatively, if we compare the X-ray flux level with the expectation from the X-ray to MIR relation in Stern (2015) (here we obtain the MIR luminosity from interpolating the *WISE* data shown in Figure 3), the first *Chandra* observation is also X-ray weak by a factor of ≈ 16 , and the second *Chandra* observation follows the empirical relation well.

radio-quiet non-BAL quasar known to show such extreme X-ray variability, and like SDSS J1539+3954 it varied between an X-ray weak state and an X-ray normal state. SDSS J1539+3954 has $\log L_{\text{bol}} \approx 47.17$ (Shen et al. 2011), which is even more luminous (by a factor of ≈ 3) than PHL 1092. The discovery of extreme X-ray variability from SDSS J1539+3954, combined with the PHL 1092 results, suggests that weak UV emission lines may be a good indicator for finding extreme X-ray variability events among luminous radio-quiet quasars.

4.2. Possible Explanations for Extreme X-Ray Variability Events

We have proposed a thick inner accretion-disk model to explain the multiwavelength properties of WLQs (e.g., Figure 1 of Ni et al. 2018), which also has the potential to explain this extreme X-ray variability event. Simulations and analytical models suggest that for quasars with high Eddington ratios, geometrically thick inner accretion disks with high column densities are expected (e.g., Abramowicz et al. 1988; Jiang et al. 2014, 2019; Wang et al. 2014). Dense outflows arise with these thick disks in simulations (e.g., Jiang et al. 2014, 2019), and we implicitly include any associated dense outflow within the term “thick disk” throughout. The thick inner accretion disk can prevent ionizing X-ray/EUV photons from reaching an equatorially concentrated high-ionization broad emission-line region (BLR), while the UV/optical photons from the disk itself remain unobscured. Thus, weak high-ionization emission lines are observed. When our line of sight (to the central X-ray source) intercepts the thick inner accretion disk for a given WLQ, we observe an X-ray weak WLQ; when it misses this shield, we observe an X-ray normal WLQ.

As predicted in Section 6.2 of Luo et al. (2015), in the context of this model, the observed extreme X-ray variability event could be caused by a slight change in the thickness of the disk that moved across our line of sight.²⁰ This could arise due to rotation of a thick inner disk that is somewhat azimuthally asymmetric, or alternatively due to small changes in the inner-disk structure itself (e.g., see Figure 3 of Jiang et al. 2019). If the change in the disk thickness is slight, there will be no significant change in the BLR illumination and UV/optical photon emission to affect the UV emission-line and continuum properties.²¹

Ross & Fabian (2005) have also proposed a reflection model that has the potential to explain this extreme X-ray variability event, where the X-ray variability is driven by gravitational light-bending effects. Such effects can change the amount of X-ray emission reaching an observer when the distance

²⁰ Liu et al. (2019) proposed that a change in the height/size of the corona can also cause extreme X-ray variability in the presence of the thick disk via the same mechanism (as changes in both the disk thickness and the corona height/size are changes in the relative positions of the disk edge and the central X-ray source), though the detailed physics of the corona and how the corona varies its height/size is not generally understood.

²¹ We note that it is also possible that the observed weak C IV line emission in the HET spectrum does not fully correspond to the X-ray normal state, as the average time lag between the C IV line emission and the ionizing continuum could reach $\approx 1-2$ yr in the observed frame for SDSS J1539+3954 (e.g., Grier et al. 2019). We think this possibility is not very likely, as the X-ray flux could have risen at any time in the six-year gap between the two *Chandra* observations, and while the closer half of the BLR responds to ionizing photons more promptly than the expected average lag, we do not observe any sign of stronger C IV. Future spectroscopic monitoring is needed to give a definite answer.

between the primary X-ray source and the central black hole changes, causing the observed X-ray variability (Miniutti & Fabian 2004). However, in the context of this reflection model, it is not clear why extreme X-ray variability would have any particular link with WLQs.

5. Conclusions and Future Work

We have reported a dramatic increase in the X-ray flux of a luminous WLQ, SDSS J1539+3954, by a factor of $\gtrsim 20$. We obtained a contemporaneous HET spectrum of SDSS J1539+3954 after observing this X-ray flux rise with *Chandra*. We found that its overall UV continuum and emission-line properties do not show significant changes compared with previous SDSS and BOSS spectra.

We propose that the extreme X-ray variability event can be explained by a thick inner accretion-disk model with a slight change in the thickness of the disk, or a reflection model where strong gravitational light bending occurs. We also note that the most-luminous radio-quiet AGNs showing extreme X-ray variability are all WLQs, which may suggest a link between weak emission lines and extreme X-ray variability.

X-ray monitoring of a sample of WLQs will help constrain the frequency, duration, and amplitude of such extreme X-ray variability events, which can probe the possible scenarios listed in this Letter and thus clarify AGN accretion physics in general. For example, if extreme X-ray variability is caused by slight changes in the disk thickness, then this type of event should be relatively rare as we only expect such events to occur at viewing angles close to skimming the top of the thick inner disk. The smaller the change, the lower the frequency of extreme X-ray variability events we will observe.

We thank HET astronomers Steven Janowiecki and Sergey Rostopchin for help obtaining the HET spectra. We thank Greg Zeimman for help reducing the HET spectra. Q.N., W.N.B., W. Y., and J.D.T. acknowledge support from CXC grant GO8-19076, NASA ADP grant 80NSSC18K0878, and NSF grant AST-1516784. B.L. acknowledges NSFC grant 11673010. F. V. acknowledges financial support from CONICYT and CASSACA through the Fourth call for tenders of the CAS-CONICYT Fund, CONICYT grants BasalCATA AFB-170002. P.H. acknowledges NSERC grant 2017-05983.

ORCID iDs

Q. Ni  <https://orcid.org/0000-0002-8577-2717>
 W. Yi  <https://orcid.org/0000-0001-9314-0552>
 B. Luo  <https://orcid.org/0000-0002-9036-0063>
 J. D. Timlin, III  <https://orcid.org/0000-0001-8131-1801>
 P. B. Hall  <https://orcid.org/0000-0002-1763-5825>
 Hezhen Liu  <https://orcid.org/0000-0003-0582-9558>
 R. M. Plotkin  <https://orcid.org/0000-0002-7092-0326>
 O. Shemmer  <https://orcid.org/0000-0003-4327-1460>
 F. Vito  <https://orcid.org/0000-0003-0680-9305>

References

- Abramowicz, M. A., Czerny, B., Lasota, J. P., & Szuszkiewicz, E. 1988, *ApJ*, **332**, 646
 Arnaud, K. A. 1996, in ASP Conf. Ser. 101, XSPEC: The First Ten Years, ed. G. H. Jacoby & J. Barnes (San Francisco, CA: ASP), 17
 Bellm, E. C., Kulkarni, S. R., Graham, M. J., et al. 2019, *PASP*, **131**, 018002
 Carnerero, M. I., Raiteri, C. M., Villata, M., et al. 2017, *MNRAS*, **472**, 3789
 Cash, W. 1979, *ApJ*, **228**, 939

- Chonis, T. S., Hill, G. J., Lee, H., Tuttle, S. E., & Vattiat, B. L. 2014, *Proc. SPIE*, **9147**, 91470A
- Dawson, K. S., Schlegel, D. J., Ahn, C. P., et al. 2013, *AJ*, **145**, 10
- Diamond-Stanic, A. M., Fan, X., Brandt, W. N., et al. 2009, *ApJ*, **699**, 782
- Drake, A. J., Djorgovski, S. G., Mahabal, A., et al. 2009, *ApJ*, **696**, 870
- Fan, X., Strauss, M. A., Gunn, J. E., et al. 1999, *ApJL*, **526**, L57
- Fruscione, A., McDowell, J. C., Allen, G. E., et al. 2006, *Proc. SPIE*, **6270**, 62701V
- Garmire, G. P., Bautz, M. W., Ford, P. G., Nousek, J. A., & Ricker, George R., Jr. 2003, *Proc. SPIE*, **4851**, 28
- Gibson, R. R., & Brandt, W. N. 2012, *ApJ*, **746**, 54
- Gibson, R. R., Brandt, W. N., & Schneider, D. P. 2008, *ApJ*, **685**, 773
- Grier, C. J., Shen, Y., Horne, K., et al. 2019, *ApJ*, **887**, 38
- Jiang, Y.-F., Stone, J. M., & Davis, S. W. 2014, *ApJ*, **796**, 106
- Jiang, Y.-F., Stone, J. M., & Davis, S. W. 2019, *ApJ*, **880**, 67
- Just, D. W., Brandt, W. N., Shemmer, O., et al. 2007, *ApJ*, **665**, 1004
- Kraft, R. P., Burrows, D. N., & Nousek, J. A. 1991, *ApJ*, **374**, 344
- Liu, H., Luo, B., Brandt, W. N., et al. 2019, *ApJ*, **878**, 79
- Luo, B., Brandt, W. N., Hall, P. B., et al. 2015, *ApJ*, **805**, 122
- Lusso, E., & Risaliti, G. 2016, *ApJ*, **819**, 154
- Mainzer, A., Bauer, J., Cutri, R. M., et al. 2014, *ApJ*, **792**, 30
- Marlar, A., Shemmer, O., Anderson, S. F., et al. 2018, *ApJ*, **865**, 92
- Martin, D. C., Fanson, J., Schiminovich, D., et al. 2005, *ApJL*, **619**, L1
- Middei, R., Vagnetti, F., Bianchi, S., et al. 2017, *A&A*, **599**, A82
- Miniutti, G., Brandt, W. N., Schneider, D. P., et al. 2012, *MNRAS*, **425**, 1718
- Miniutti, G., & Fabian, A. C. 2004, *MNRAS*, **349**, 1435
- Ni, Q., Brandt, W. N., Luo, B., et al. 2018, *MNRAS*, **480**, 5184
- Oknyansky, V. L., Winkler, H., Tsygankov, S. S., et al. 2019, *MNRAS*, **483**, 558
- Park, T., Kashyap, V. L., Siemiginowska, A., et al. 2006, *ApJ*, **652**, 610
- Plotkin, R. M., Anderson, S. F., Brandt, W. N., et al. 2010, *AJ*, **139**, 390
- Ponti, G., Papadakis, I., Bianchi, S., et al. 2012, *A&A*, **542**, A83
- Ramsey, L. W., Adams, M. T., Barnes, T. G., et al. 1998, *Proc. SPIE*, **3352**, 34
- Reeves, J. N., Turner, M. J. L., Ohashi, T., & Kii, T. 1997, *MNRAS*, **292**, 468
- Richards, G. T., Lacy, M., Storrie-Lombardi, L. J., et al. 2006, *ApJS*, **166**, 470
- Ross, R. R., & Fabian, A. C. 2005, *MNRAS*, **358**, 211
- Saez, C., Brandt, W. N., Gallagher, S. C., Bauer, F. E., & Garmire, G. P. 2012, *ApJ*, **759**, 42
- Scott, A. E., Stewart, G. C., Mateos, S., et al. 2011, *MNRAS*, **417**, 992
- Shemmer, O., Brandt, W. N., Vignali, C., et al. 2005, *ApJ*, **630**, 729
- Shen, Y., & Kelly, B. C. 2012, *ApJ*, **746**, 169
- Shen, Y., Richards, G. T., Strauss, M. A., et al. 2011, *ApJS*, **194**, 45
- Skrutskie, M. F., Cutri, R. M., Stiening, R., et al. 2006, *AJ*, **131**, 1163
- Steffen, A. T., Strateva, I., Brandt, W. N., et al. 2006, *AJ*, **131**, 2826
- Stern, D. 2015, *ApJ*, **807**, 129
- Timlin, J. D., Brandt, W. N., Ni, Q., et al. 2020, *MNRAS*, **492**, 719
- Vanden Berk, D. E., Richards, G. T., Bauer, A., et al. 2001, *AJ*, **122**, 549
- Wang, J.-M., Qiu, J., Du, P., & Ho, L. C. 2014, *ApJ*, **797**, 65
- Wright, E. L., Eisenhardt, P. R. M., Mainzer, A. K., et al. 2010, *AJ*, **140**, 1868
- Wu, J., Brandt, W. N., Anderson, S. F., et al. 2012, *ApJ*, **747**, 10
- Wu, J., Brandt, W. N., Hall, P. B., et al. 2011, *ApJ*, **736**, 28
- Yang, G., Brandt, W. N., Luo, B., et al. 2016, *ApJ*, **831**, 145
- Yi, W., Vivek, M., Brandt, W. N., et al. 2019, *ApJL*, **870**, L25
- York, D. G., Adelman, J., Anderson, J. E., Jr., et al. 2000, *AJ*, **120**, 1579